

4D Printing of Hygroscopic Liquid Crystal Elastomer Actuators

Keumbee Kim, Yuanhang Guo, Jaehee Bae, Subi Choi, Hyeong Yong Song, Sungmin Park, Kyu Hyun, and Suk-Kyun Ahn*

Liquid crystal elastomers (LCEs) are broadly recognized as programmable actuating materials that are responsive to external stimuli, typically heat or light. Yet, soft LCEs that respond to changes in environmental humidity are not reported, except a few examples based on rigid liquid crystal networks with limited processing. Herein, a new class of highly deformable hygroscopic LCE actuators that can be prepared by versatile processing methods, including surface alignment as well as 3D printing is presented. The dimethylamino-functionalized LCE is prepared by the aza-Michael addition reaction between a reactive LC monomer and N,N'-dimethylethylenediamine as a chain extender, followed by photopolymerization. The humidity-responsive properties are introduced by activating one of the LCE surfaces with an acidic solution, which generates cations on the surface and provides asymmetric hydrophilicity to the LCE. The resulting humidity-responsive LCE undergoes programmed and reversible hygroscopic actuation, and its shape transformation can be directed by the cut angle with respect to a nematic director or by localizing activation regions in the LCE. Most importantly, various hygroscopic LCE actuators, including (porous) bilayers, a flower, a concentric square array, and a soft gripper, are successfully fabricated by using LC inks in UV-assisted direct-ink-writing-based 3D printing.

cones,^[1] twisting of orchid tree seed pods,^[2] bending of wheat awns,^[3] self-burrowing of seeds,^[4] and expansion/contraction of bacterial spores.^[5] Inspired by such natural materials, various types of water- and/or humidity-responsive actuators, often designed as bilayers, have been developed by incorporating hydrophilic organic or inorganic components, e.g., hydrogels,^[6] hydrophilic polymers,^[7] cellulose nanocrystals (CNCs),^[8] graphene oxide,^[9] microbes,^[10] and nanoporous silica.^[11] The ability of humidity-responsive actuators to convert the ubiquitous presence of humidity in ambient air into mechanical motion afford the advantages of being low-cost, harmless, and actuating under mild conditions compared to thermal- or photoactuators; therefore, these actuators are attractive for application in sensors,^[12] smart windows,^[13] weather-responsive architectures,^[14] smart textiles,^[10,15] soft robots,^[16] and energy-harvesting devices.^[17]

1. Introduction

Shape transformation in response to water or humidity occurs in numerous biological systems, such as opening of pine-

Liquid crystal networks (LCNs) or liquid crystal elastomers (LCEs) are crosslinked LC polymers which are widely known as actuating materials under external stimuli that can change the molecular alignment.^[18] Macroscopic deformation of LCNs and LCEs can be achieved with a predefined direction through control of director profiles that is the most prominent advantage over other types of soft materials. Moreover, unlike other soft actuators such as hydrogels or shape memory polymers which require an aqueous environment for operation or mechanical programming for temporarily deformed shape, respectively, LCE actuators can exhibit the large reversible shape change in solid state and do not require mechanical programming if they are crosslinked in a molecularly aligned state. Water- or humidity-responsive properties can also be integrated into LC polymers using several strategies.^[19] Broer and co-workers first reported a single-layer, humidity-responsive LCN containing carboxylic acid groups.^[19g,20] A subsequent alkaline treatment disrupted the hydrogen bonds in the LCN and generated carboxylate sodium salts, making the LCN hygroscopic and humidity-sensitive. The local treatment of the LCN by an alkaline solution enabled the design of shape-programmable humidity-responsive actuators that can bend, fold, and curl.^[19b] Schenning and co-workers had exploited a bilayer approach to fabricate humidity-responsive actuators by spray-coating LC mixtures containing carboxylic acids on an oriented polyamide-6

K. Kim, Y. Guo, J. Bae, S. Choi, Prof. S.-K. Ahn
Department of Polymer Science and Engineering
Pusan National University
Busan 46241, Republic of Korea
E-mail: skahn@pusan.ac.kr

Dr. H. Y. Song
Institute for Environment and Energy
Pusan National University
Busan 46241, Republic of Korea

Dr. H. Y. Song, Prof. K. Hyun
School of Chemical Engineering
Pusan National University
Busan 46241, Republic of Korea

Dr. S. Park
Advanced Materials Division
Korea Research Institute of Chemical Technology
Daejeon 34114, Republic of Korea

 The ORCID identification number(s) for the author(s) of this article can be found under <https://doi.org/10.1002/smll.202100910>.

DOI: 10.1002/smll.202100910

substrate, followed by photopolymerization.^[19a,d,21] Ware and co-workers reported a water-responsive bilayer, consisting of hydrophilic poly(ethylene glycol) and a LCE, in which complex shape changes in response to water were directed by the mechanically anisotropic LCE layer.^[19f] As an alternative strategy, Ryabchun et al. developed humidity-responsive actuators by infiltrating LC mixtures into the porous polypropylene, followed by photopolymerization.^[19c] Recently, dual-responsive LC actuators that are sensitive to moisture as well as additional external stimuli, including temperature,^[19f,21] light,^[19h,22] and SO₂ gas^[19e] have been reported to provide multiple functions.

The above-mentioned humidity-responsive LC actuators primarily rely on LCNs containing carboxylic acid groups. However, the dense networks of crosslinked chains in these LCNs hinder large deformation, and thus, make the system brittle. In addition, the fabrication methods for LCN-based actuators are limited to surface alignment; therefore, LCNs are mostly available as thin films (<30 μm). LCEs are more deformable and have more versatile processing conditions than LCNs; therefore, they can be fabricated into various geometries, including 0D particles,^[23] 1D fibers,^[24] 2D films,^[25] and complex 3D shapes.^[26] Therefore, the development of a new class of humidity-responsive actuators based on LCEs is highly desirable to overcome the aforementioned challenges associated with LCNs.

In this study, we developed a facile method to create a hygroscopic LCE actuator, which can undergo reversible and programmed shape transformation in response to changes in humidity. Unlike previously reported LCNs of which humidity-response was commonly induced by the generation of anions on the surface of the film, we introduced a new hydration method that can provide the humidity response by generating cations on the surface of the LCE film. Most importantly, it is the first time to create hygroscopic LCE actuator by direct-ink-writing (DIW)-based 3D printing, which dramatically expands complex LCE geometries accessible compared to previously reported LCN systems of which preparation was limited by surface alignment. Various types of hygroscopic LCE actuators that can mimic biological systems and soft robotic functions were fabricated by integrating different types of LCEs into a single actuator system via 3D printing.

2. Results and Discussion

2.1. Synthesis and Characterization of Liquid Crystal Elastomers

Humidity-responsive LCEs, referred to h-LCE hereafter, were prepared by chain extending a reactive LC monomer (RM82) with *N,N*-dimethylethylenediamine (DMEN) via aza-Michael addition, and subsequent photopolymerization, yielding a dimethylamino-functionalized LCE (Figure 1a). The number-average molecular weight (*M_n*) of the humidity-responsive LC oligomer (h-LCO) after chain extension was 6900 g mol⁻¹, as determined by ¹H NMR end-group analysis, similar to our previous report (Figure S1, Supporting Information).^[27] To prepare a monodomain h-LCE (i.e., a planar-aligned h-LCE), the reactions were performed inside a surface-aligned cell, as shown in Figure 1b. The gel fraction of the h-LCE was 90%, suggesting sufficient crosslinking. The macroscopic alignment of the

monodomain h-LCE was verified by observing director orientation under polarized optical microscope (POM), as shown in Figure 1c. The X-ray scattering measurements at small and wide angles revealed nematic phase with smectic-C type fluctuations (cybotactic order) in the monodomain h-LCE,^[28] with parameters of *d* = 39.3 Å, β = 32°, and *L* = 46.3 Å, where *d* is a layer spacing by *d* = 2π/*q_o*, β is molecular tilt angle, and *L* = *d*/cosβ is the molecular length, respectively (Figure 1d). From the wide-angle x-ray scattering (WAXS) results (Figure S2, Supporting Information), the intermolecular distance *d_i* was determined as 4.49 Å and the order parameter (*S*) was calculated to be 0.29.

2.2. Thermal, Mechanical and Viscoelastic Properties

The thermal properties of h-LCO and h-LCE were determined using second heating curves of differential scanning calorimetry (DSC) as shown in Figure 2a. Both glass transition temperature (*T_g*, -15 °C) and nematic-isotropic transition temperature (*T_{ni}*, 93 °C, Δ*H* = 1.3 J g⁻¹) were clearly identified for h-LCO, while only *T_g* (2 °C) was detected for h-LCE due to the restriction of its chain network.^[25a,26a] The mechanical properties of monodomain h-LCE, investigated by stress-strain measurement at 30 °C, revealed anisotropic nature: a relatively stiff (*E* ≈ 38 MPa) and brittle (ε ≈ 21%) along the director orientation, and a soft (*E* ≈ 9.9 MPa) and deformable (ε ≈ 193%) in perpendicular to the director orientation (Figure 2b). The viscoelastic properties of the polydomain h-LCE, investigated by dynamic mechanical analysis (DMA) revealed a *T_g* of 21 °C, which is 19 °C higher than that determined by DSC (Figure 2c). After glass transition, a rubbery plateau was observed, indicating efficient formation of chain networks. Based on the rubbery modulus (2.04 MPa at 150 °C), the crosslinking density (*ν_e*) was calculated using the following equation

$$\nu_e = \frac{E'}{3RT} \quad (1)$$

where *E'* is storage modulus at 150 °C, *R* is the gas constant, and *T* is the temperature (in K). The *ν_e* value of LCE was 1.93 × 10⁻⁴ mol cm⁻³, which is comparable to the other LCEs prepared by similar polymerization method.^[25c,29] The thermal, mechanical, and viscoelastic properties indicate that h-LCE is chemically crosslinked, elastomeric, and can be mechanically anisotropic for monodomain h-LCE.

2.3. Surface Activation

The dimethylamino groups in polymers can be easily quaternized by treating with low-pH solutions or with alkyl halides, which allows for the creation of cationic polymers.^[30] Inspired by such studies, dimethylamino groups in h-LCE are exploited to generate cations on the h-LCE surface. Similar to a previously reported method,^[19b] only one side of a monodomain h-LCE film was placed in contact with an acidic solution (0.1 M, HCl (aq)) for 3 min (activation), as shown schematically in Figure 3a. Charge generation on the activated h-LCE surface

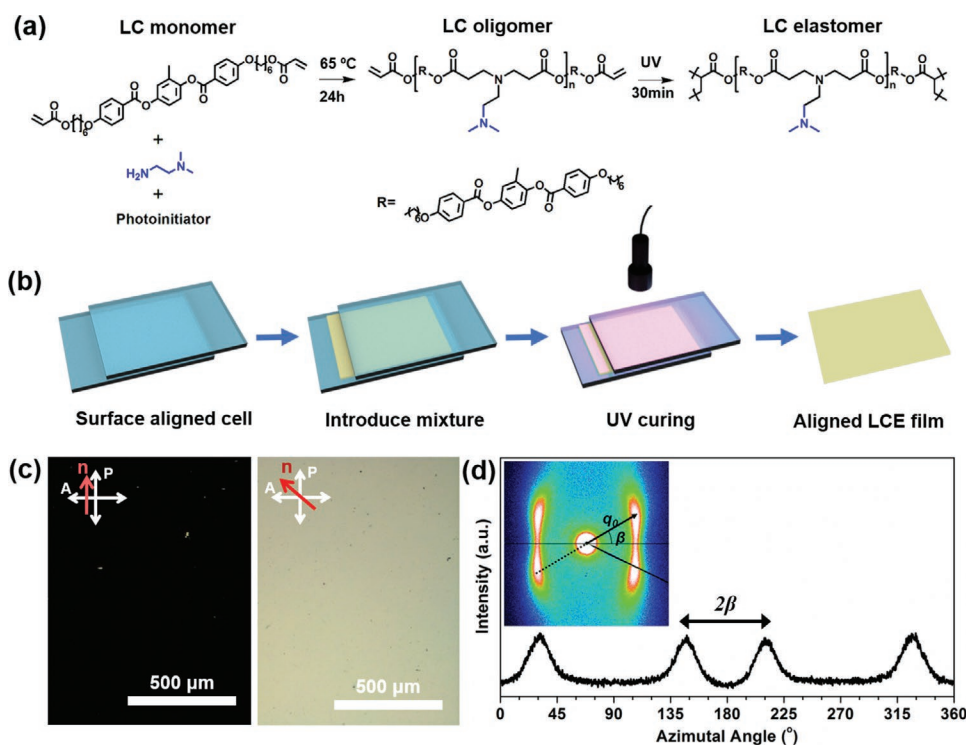


Figure 1. a) Reaction scheme of h-LCE by chain extension of the LC monomer by aza-Michael addition reaction and photopolymerization. b) Fabrication of a surface-aligned h-LCE film. c) POM images of a monodomain h-LCE film. d) 1D azimuthal scan profile at $q_0 = 0.160 \text{ \AA}^{-1}$ and 2D SAXS pattern (inset) of the monodomain h-LCE film at room temperature.

was confirmed by contact angle measurement and Fourier-transform infrared (FTIR) spectroscopic analyses. After activation, the contact angle of h-LCE decreases considerably from 96° to 62° , suggesting an increase in the hydrophilicity of the h-LCE surface treated with the acidic solution, probably due to generation of cations (Figure 3b). The FTIR spectra before and after activation are shown in Figure 3c. The two peaks at 2750 and 2850 cm^{-1} , corresponding to $-\text{N}(\text{CH}_3)_2$ stretching, disappear after activation, which implies protonation of the dimethylamino groups, i.e., formation of $-\text{NH}^+(\text{CH}_3)_2$. The stronger electron-withdrawing effect of $-\text{NH}^+(\text{CH}_3)_2$ shifts these two peaks to a higher wavenumber, merging them with other peaks at 2940 cm^{-1} .^[31] Moreover, a broad peak at 3420 cm^{-1} appears after activation, attributed to the adsorption of moisture on

the h-LCE surface. The HCl penetration occurs only within a thin surface layer of h-LCE, of which penetration depth is about $5 \mu\text{m}$ out of total $50 \mu\text{m}$ thickness as supported by scanning electron microscopy (SEM) and energy-dispersive spectrometer (EDS) analyses (Figure S3, Supporting Information). Comparable value of the penetration depth in the humidity-responsive LCN treated with KOH solution was recently reported by Lan et al.^[19e]

2.4. Surface Alignment and Hygroscopic Actuation

The increase in hydrophilicity on one surface of h-LCE after activation induces asymmetric moisture sensitivity to the

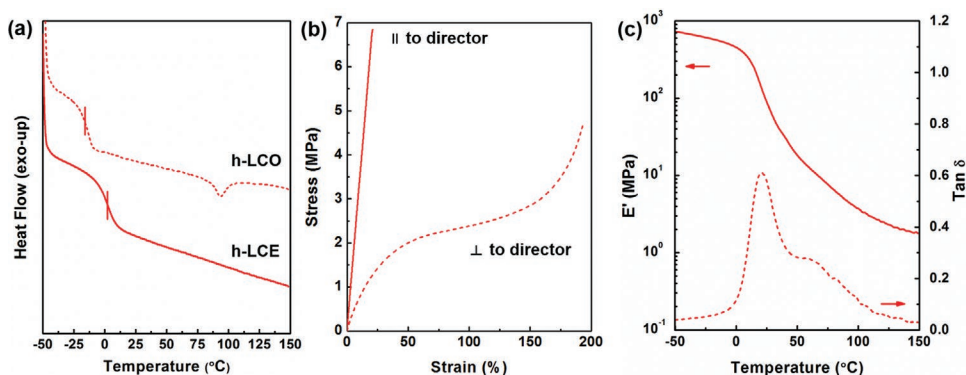


Figure 2. a) DSC thermograms of h-LCO and h-LCE during the second heating cycle at a heating rate of $10 \text{ }^\circ\text{C min}^{-1}$. b) Stress-strain curves of a monodomain h-LCE parallel and perpendicular to the nematic director. c) Viscoelastic properties of a polydomain h-LCE.

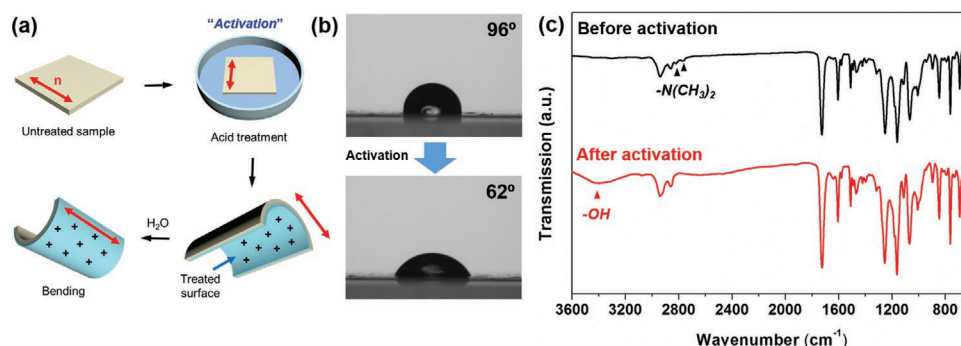


Figure 3. a) Schematic of monodomain h-LCE activation by acidic solution (0.1 M HCl) and its bending behavior upon exposure to moisture. b) Contact angles of an h-LCE before and after activation. c) FTIR spectra of an h-LCE before and after activation.

h-LCE. In other words, the activated surface can swell significantly upon exposure to moisture, while the inactivated surface remains hydrophobic and unresponsive to moisture. Therefore, the activated h-LCE film can bend toward the inactivated surface when immersed in water or exposed to moisture, due to the stress gradient developed through the film thickness (Figure 3a). The direction of bending is guided by the anisotropic stiffness of h-LCE. As observed in the stress–strain curve, the elastic modulus of h-LCE film is 3.8 times greater along the nematic director (n) than that perpendicular to the nematic director. The strong anisotropic mechanical properties of h-LCE film were not significantly changed after activation (Figure S4, Supporting Information). Consequently, the h-LCE film expands more in the direction perpendicular to the nematic director (i.e., softer part) when exposed to moisture.

The shape change of the h-LCE film is also strongly influenced by the cut angle with respect to nematic director. For demonstration, three h-LCE films with the same initial geometry (length \times width \times thickness = 18 mm \times 2 mm \times 0.05 mm) were prepared by cutting a monodomain h-LCE film at 0°, 45°, and 90° with respect to the nematic director, as shown in Figure 4a(i). When immersed in water, each sample underwent distinct shape transformations, forming a tube, a helical ribbon, and a spiral shape for 0°, 45°, and 90°, respectively (Figure 4a(iii)), due to the different directions of anisotropic swelling generated in the different samples, as schematically proposed in Figure 4a(ii). We note that some extent of pre-bend was observed after activation and subsequent drying, with bending direction toward activated side along the nematic director. Such pre-bend indicates the shrinkage of activated side which may be associated with the slight decrease in molecular order by the charge generation. Similar observations of the shrinkage in the humidity-responsive LCNs were previously reported by Schenning and co-workers.^[19b,h] To validate our results, several control experiments were performed, and the results are summarized in Table S1 (Supporting Information). When monodomain h-LCE was inactivated or when both surfaces of h-LCE were activated, no apparent shape changes were observed upon immersing in water. These results suggest that the asymmetric moisture sensitivity of h-LCE is critical for providing hygroscopic actuation. Also, the activated polydomain h-LCE films exhibited uncontrolled shape changes when immersed in water, implying the importance of global molecular orientation to achieve controlled shape changes. Finally,

a monodomain LCE chain-extended by *n*-butyl amine (*n*-BA), referred to as t-LCE hereafter due to its intrinsic thermally induced shape-changing properties, was prepared by following a protocol similar to that in our previous report^[25d] and was activated by the acidic solution. However, no water-responsive shape change was observed, indicating the importance of dimethylamino groups in h-LCE.

For quantitative analyses of the hygroscopic actuations of h-LCEs, a custom-made humidity chamber was prepared, in which dry and humid conditions can be precisely controlled and monitored by a hygrometer (Figure S5, Supporting Information). The bending and twisting of h-LCEs with increasing relative humidity (RH) were monitored, and the representative photographs are shown in Figure 4b,c, respectively, and the corresponding videos can be found in Videos S1 and S2 (Supporting Information). On the one hand, the h-LCE film cut at 90° with respect to the nematic director gradually bended with increasing RH and eventually became coiled. On the other hand, the h-LCE film cut at 45° with respect to the nematic director initially adopted a negative, right-hand twisting at low RH, which gradually changed to a positive, right-hand twisting with higher twisting degree at higher RH. By analyzing the frames from the video at different humidity levels, the bending curvature was calculated using the following equation

$$\kappa = \frac{1}{r} \quad (2)$$

where κ is the curvature (mm⁻¹) and r is the bending radius (mm). The twisting degree was quantified in half turns (180°) of the film by examining frames from the video, where a half turn is defined by the flipping of a face of the film from front to back.^[32] Figure 4d shows that both the bending and twisting degrees of h-LCEs start to increase after 40% RH, accelerate in the range 50–80% RH and tend to saturate at above 85% RH. To evaluate the actuation stability further, the curvature of bending and unbending of h-LCE was examined by switching RH between 30% and 80% over multiple cycles. Figure 4e shows that after the first cycle, the curvature of bending and unbending between 30% and 80% RH remains fairly stable, even after 14 cycles.

Complex and reversible shape changes are further demonstrated by localizing the activation area in h-LCE films. As an example, to obtain the shapes of the letters “P,” “N,” and “U,”

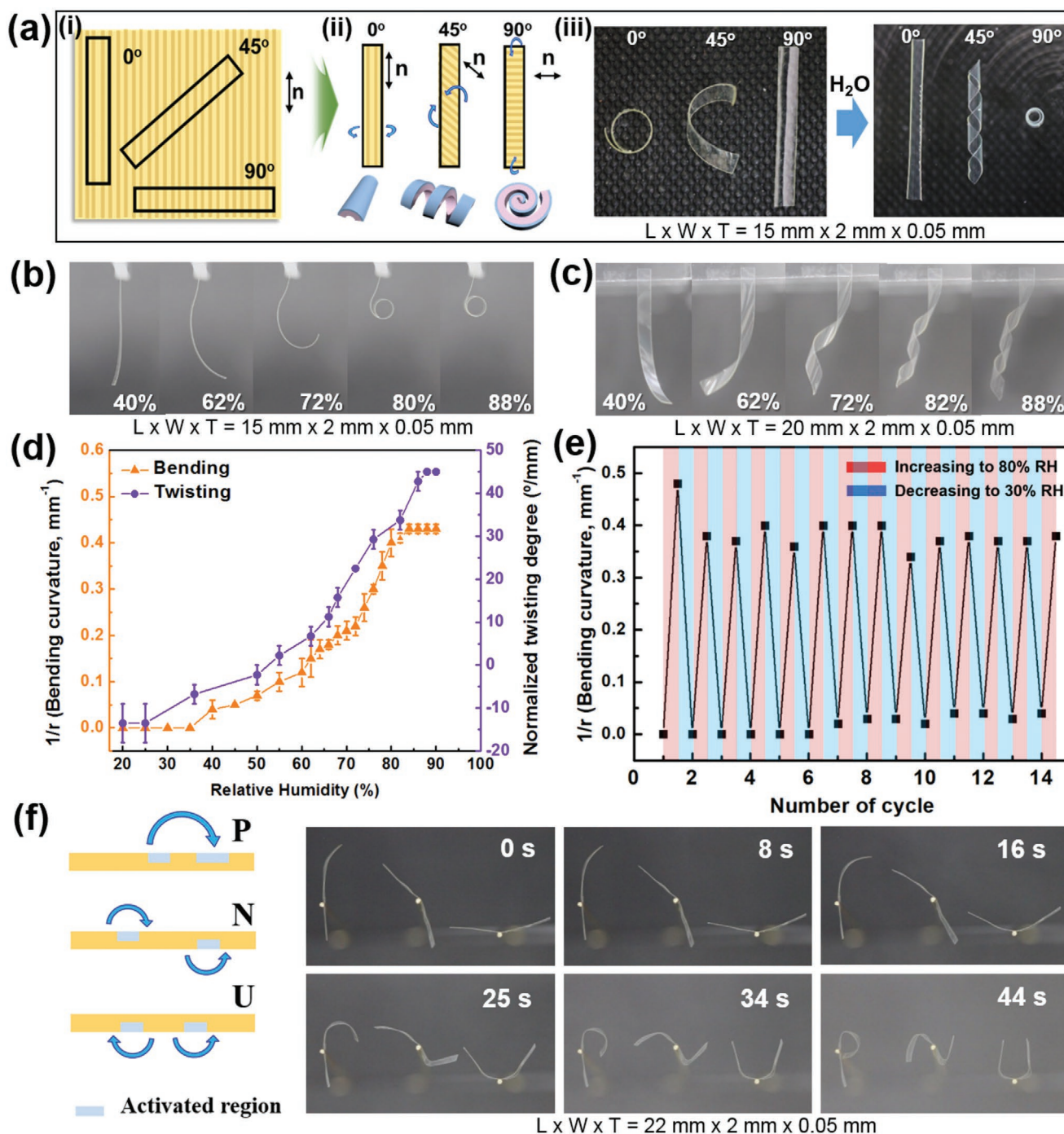


Figure 4. a-i) Schematic of preparing h-LCE films by cutting a monodomain h-LCE film at different angles with respect to the nematic director, a-ii) the proposed shape changes of h-LCEs under moisture, depending on the cut angles with respect to nematic director, and a-iii) shape changes of h-LCEs before and after immersing in water. b) Bending and c) twisting of h-LCEs under different relative humidity conditions at room temperature. d) Degrees of bending and twisting of h-LCEs as functions of relative humidity. e) Changes in the bending curvature of an h-LCE between 30% and 80% over 14 cycles. f) Illustration of activated regions in three h-LCE films to obtain the shapes of letters "P," "N," and "U," and photographs taken during transforming into the desired letter shapes with increasing humidity.

the acronym for Pusan National University, the blue regions in h-LCE films (Figure 4f) are carefully treated with the acidic solution using a cotton swab: i) two distinct areas with different sizes were activated on the top of an h-LCE film for the letter "P," ii) two distinct areas of the same size, but on opposite

surfaces of the h-LCE film, were activated for the letter "N," and iii) two distinct areas of the same size on the bottom of the h-LCE film were activated for the letter "U." With increasing RH, each h-LCE film transforms into the desired letter shapes within 44 s (Figure 4f and Video S3, Supporting Information).

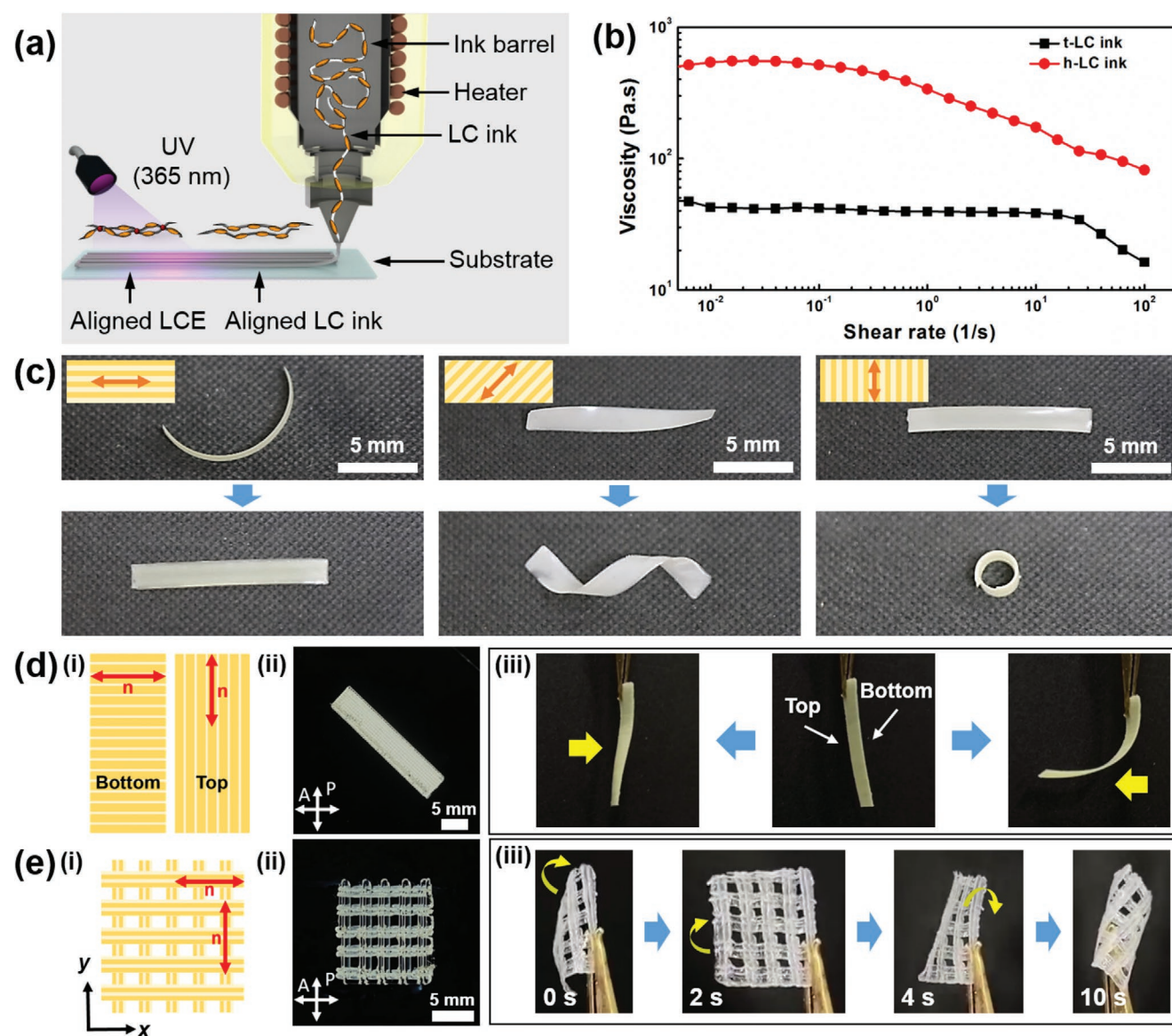


Figure 5. a) Schematic of DIW-based 3D printing of LC ink, and subsequent UV crosslinking to produce an LCE. b) Steady shear viscosities of h-LC and t-LC inks as functions of shear rate. c) 3D-printed h-LCE films extruded at different printing directions, indicated by double-headed arrows (top row), and their programmed shape changes upon exposure to moisture (bottom row). d-i) Schematic of the printing path of a h-LCE rectangular bilayer, d-ii) an image of the printed bilayer observed between crossed polarizers, and d-iii) semi-bidirectional bending of the rectangular bilayer where yellow arrows indicate the incoming direction of humidifying source. e-i) Schematic of the printing path of a h-LCE porous bilayer, e-ii) an image of the printed porous bilayer observed between crossed polarizers, and e-iii) hygroscopic actuation when exposed to a humidifying source.

2.5. Direct-Ink-Writing and Hygroscopic Actuation

Unlike previously reported humidity-responsive LCNs, which were prepared by directly photopolymerizing LC monomers on the aligned substrates, the procedure to prepare our h-LCE involved oligomerization, producing viscous h-LCO (or h-LC ink) as an intermediate product. Recently, various types of LCOs have been successfully used as LC inks for DIW-based 3D printing,^[26b,c,29a,33] and the resulting 4D-printed LCEs can be actuated by heat or light. Intriguingly, our h-LC ink also showed excellent chain alignment during DIW-based 3D printing through a combination of shear force during extrusion and elongational flow during deposition on a substrate. The printing

conditions, including temperature, pressure, and printing rate, were carefully optimized to achieve high alignment of the h-LC ink, and to avoid under-extrusion or over-extrusion. The optimized maps for printing conditions and representative POM images are shown in Figure S6 (Supporting Information). The h-LC ink extruded into a predesigned shape could be effectively fixed by photocrosslinking the remaining acrylates in the h-LC ink (Figure 5a). The rheological behavior of h-LC ink ($M_n \approx 6000 \text{ g mol}^{-1}$) exhibits shear thinning when extruded in a nematic phase (60°C), indicating that h-LC ink undergoes chain orientation at high shear rate. Interestingly, the shear viscosity of h-LC ink is about one order of magnitude higher than that of t-LC ink ($M_n \approx 5100 \text{ g mol}^{-1}$) chain-extended

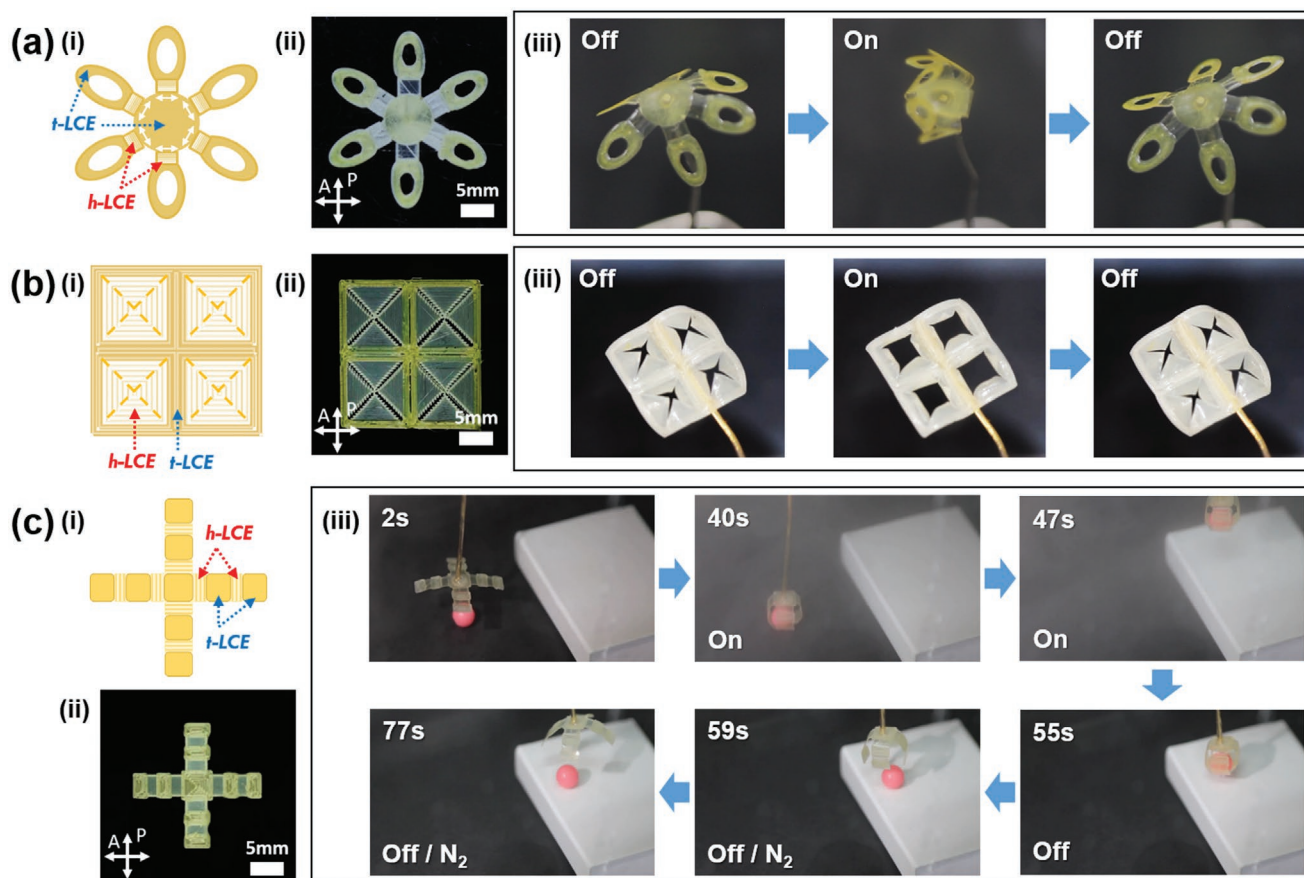


Figure 6. a-i) Schematic of the printing path of a h-LCE flower, a-ii) an image of the printed structure observed between crossed polarizers, and a-iii) hygroscopic actuation under dry (Off) and humid (On) conditions. b-i) Schematic of the printing path of a 2×2 array of concentric square-patterned h-LCE, where the dashed lines describe the cross-cut, b-ii) an image of the printed structure observed between crossed polarizers, and b-iii) hygroscopic actuation under dry (Off) and humid (On) conditions. c-i) A schematic of the printing path of LCE soft gripper, integrating both h-LCE and t-LCE. c-ii) An image of the printed structure observed between crossed polarizers. c-iii) Soft robotic functions of the LCE gripper (i.e., grabbing (40 s), transporting (47 s), holding (55 s), and releasing (59 s) an object), achieved by humidity control.

by n-BA (Figure 5b), which may be related to the intermolecular interactions due to the presence of polar dimethylamino groups.^[34]

By taking advantage of complex structural design by 3D printing, various forms of 3D-printed h-LCEs were prepared, and their hygroscopic actuations were explored. First, three h-LCE films having the same dimensions (length \times width \times thickness = 25 mm \times 3 mm \times 0.1 mm), but with different molecular orientations, were printed by simply adjusting the printing path. After activation and exposure to high humidity, h-LCE films underwent distinct shape changes depending on the printing path, similar to h-LCE films prepared by surface alignment followed by cutting at a particular angle (Figure 5c). This result suggested that programmed shape changes in response to moisture can also be achieved by 3D-printed h-LCEs, but in a more straightforward manner with larger sample thickness than the samples prepared by surface alignment. Second, printing and actuation of h-LCE bilayers were demonstrated. The rectangular bilayer was printed with 90° difference in orientation between the top and bottom layers, and both sides were activated (Figure 5d). Intriguingly, the bilayer underwent a distinct deformation depending on the incoming direction of humidifying source. As shown in

Figure 5d(iii) and Video S4 (Supporting Information), when the humidifying source was provided from right side, the bilayer underwent bending. However, if the humidifying source was provided from left side, the bilayer returned to a near flat state. The capability of semi-bidirectional bending is due to the orthogonal orientation between top and bottom layers of the bilayer. We also printed a porous bilayer structure where the top and bottom layers were oriented along the x - and y -axis, respectively, and selectively activated the bottom layer as shown in Figure 5e. When exposed to a humid environment, the porous bilayer started to curl up and eventually flipped over within 10 s (Figure 5e(iii) and Video S5, Supporting Information). Thus, 3D printability and programmed shape changes to environmental stimulus suggest the potential of h-LCE as 4D-printing materials.

We also demonstrated the capability of multimaterials printing with more complex structures. For example, an h-LCE flower was printed using two LC inks: the six hinges of a flower were printed using h-LC ink, and the six petals and the circular center of the flower were printed using humidity-insensitive t-LC ink. Notably, only h-LC ink was molecularly aligned to obtain controlled hygroscopic actuation, while the alignment was not critical for t-LC ink. The printing path schematic of

the h-LCE flower is illustrated in **Figure 6a(i)**, and the actual printing process can be viewed in Video S6 (Supporting Information). The image of the 3D-printed h-LCE flower observed between crossed polarizers confirmed that the desired alignment was obtained for each part of the flower (**Figure 6a(ii)**). After activation, the resulting h-LCE flower gradually closed and opened its petals under humid and dry conditions, respectively, due to the bending and unbending of the hinges (**Figure 6a(iii)** and Video S7, Supporting Information). Accordingly, our h-LCE flower successfully mimicked hygroscopic responses of motile plants, such as pine cones^[1] and morning glory flower.^[35] Moreover, a 2×2 array of concentric square-patterned h-LCE was printed, in which each square array was segmented by t-LCE, followed by cross-cutting the middle of each square array (**Figure 6b(i)**). The image of the 2×2 concentric square array, observed between crossed polarizers (**Figure 6b(ii)**), showed that the h-LCE parts in the array were uniformly aligned. The activated 2×2 concentric square array could switch between open and closed states depending on the humidity level (**Figure 6b(iii)** and Video S8, Supporting Information), which may be applied to adaptive textiles or smart valves.

Finally, 4D-printed h-LCE has been demonstrated as a hygroscopic soft gripper, consisting of a square center and four fingers, in which each finger was segmented by two hinges. Similar to the h-LCE flower, only the hinges were fabricated with monodomain h-LCEs, and the rest of the soft gripper was fabricated with polydomain t-LCEs. The printing path schematic and the image of the printed soft gripper, observed between crossed polarizers, are shown in **Figure 6c(i),(ii)**, respectively. When exposed to humid conditions, the LCE soft gripper (86.6 mg) could grab and lift an object (89.4 mg). Interestingly, the soft gripper could hold the object for a while by maintaining the bending of its fingers even after removing the humidifying source as long as air surrounding the LCE was humid enough ($\approx 70\%$ RH, **Figure S7a**, Supporting Information). Such shape fixing ability of our hygroscopic LCE soft gripper can be advantageous over other types of soft grippers, e.g., those operated by reversible thermal actuation, in which the deformed shape instantaneously returns to the original shape upon removal of stimulus.^[29a,36] We note that the deformed shape returned to the initial shape within 60 s when the humidifying source was removed outside a humidity chamber ($\approx 20\%$ RH, **Figure S7b**, Supporting Information). After being transported to a desired place, the object can be successfully released due to unbending of the LCE fingers upon reducing humidity by supplying dry nitrogen (**Figure 6c(iii)** and Video S9, Supporting Information).

3. Conclusion

In summary, we have synthesized a new class of humidity-responsive LCEs, containing dimethylamino groups. The humidity-responsive properties could be incorporated by activating one of h-LCE surfaces with an acidic solution to generate cations, affording asymmetric hydrophilicity to the h-LCE. The anisotropic stiffness of the molecularly aligned h-LCE allowed controlled hygroscopic actuation driven by anisotropic swelling with respect to the nematic director. Programmed and reversible hygroscopic actuation was achieved by a cut angle of the aligned

h-LCE with respect to the nematic director, as well as by localizing activation areas in the h-LCE. Most interestingly, various humidity-responsive complex structures, including (porous) bilayers, a flower, a concentric square array, and a soft gripper, were successfully fabricated by employing our LC inks in UV-assisted DIW-based 3D printing. The ability to create molecularly aligned hygroscopic LCE actuators by both surface alignment and shear alignment during 3D printing will pave the way for a wide range of applications in soft robotics, biomedical tools, adaptive textiles, and responsive architectures.

4. Experimental Section

Materials: 1,4-Bis[4-(6-acryloyloxyhexyloxy)benzoyloxy]-2-methylbenzene (RM82) was purchased from Synthron Chemical. DMEN and *n*-BA were purchased from Sigma-Aldrich. Irgacure-651 (I-651) was donated by BASF Corporation.

Cell Preparation: Glass slides were cleaned with acetone and sonicated with isopropanol, followed by 10 min of plasma treatment. To prepare a monodomain LC cell, the clean glass slides were spin-coated with an Elvamide solution (0.125 wt% in methanol) and rubbed using a velvet cloth. Two rubbed glass slides were assembled with a 50- μ m spacer between them. To prepare a polydomain LC cell, the same process was performed, excluding the rubbing stage.

Synthesis of Humidity-Responsive LCE Films: The humidity-responsive LCE was synthesized by aza-Michael addition-based step-growth polymerization between RM82 and DMEN, followed by radical photocrosslinking. The molar ratio of RM82 to DMEN was set at 1.05:1, and the weight percentage of I-651 was fixed at 1.5 wt%. The LC mixture, containing RM82, DMEN, and I-651, was thoroughly mixed on a vortex, while applying external heat using a heat gun. After complete mixing, an LC cell was filled with the mixture at 105 °C (isotropic state) and oligomerized by placing it inside a convection oven at 65 °C for 24 h. After oligomerization, the cell was exposed to UV light (OmniCure S1500, $\lambda = 365$ nm, 32 mW cm⁻²) for 30 min for photocrosslinking, yielding an h-LCE film. For activation, one of the h-LCE surfaces was brought in contact with 0.1 M HCl solution for 3 min.

Printing: The 3D printing was performed on a 3D printer (Dr. INVIVO 4D, Rokit Healthcare) equipped with a hot-melt extruder using 0.4 mm diameter nozzle. The LC ink was printed on a glass slide according to programmed G-code (NewCreatorK) at a printing speed of 6 mm s⁻¹ under a pressure of 600 kPa at 60 °C. Then, the printed structure was UV-crosslinked (OmniCure S1500, $\lambda = 365$ nm, 70 mW cm⁻²) for 30 min. For the purpose of optimizing printing condition (**Figure S6**, Supporting Information), only a nozzle diameter of 0.2 mm was used because of better observation of LC alignment under POM.

Materials Characterization: ¹H NMR spectra were collected using a 500 MHz Varian spectrophotometer using CDCl₃ as the solvent. A POM (Nikon Eclipse LV100N POL), equipped with a heating stage (Linkam LTS420), was used to characterize the textures and alignment of LCEs. Differential scanning calorimetry (TA Instruments, Discovery DSC 25) was performed by heating the samples to 150 °C, then cooling to -50 °C, and reheating to 150 °C at a rate of 10 °C min⁻¹ under nitrogen flow. Attenuated total-reflectance Fourier-transform infrared (ATR-FTIR) spectra were recorded on a Jasco FT/IR-4600 spectrometer. A background spectrum (32 scans at 4 cm⁻¹ resolution) of a clean ATR crystal was used as the reference. The contact angle was measured using a Theta Lite contact angle meter (Biolin Scientific) at room temperature. The mechanical and viscoelastic properties were determined using a dynamic mechanical analyzer (TA instruments, DMA Q850) under stress-strain analysis and a temperature ramp, respectively. For stress-strain measurement, a monodomain h-LCE (length \times width \times thickness = 8.0 mm \times 4.0 mm \times 0.05 mm) was equilibrated at 30 °C under a preload of 1 mN, and the force was increased at a rate of 0.2 N min⁻¹. For viscoelastic measurement, a polydomain h-LCE (length \times width \times

thickness = 7.0 mm × 5.0 mm × 0.05 mm) was heated from −100 to 200 °C at a rate of 3 °C min^{−1} under a constant frequency of 1 Hz. Steady-shear viscosities of the LC inks were measured at 60 °C using a strain-controlled rotational rheometer (TA instruments, ARES-G2), equipped with a 25-mm parallel plate geometry. Images and videos of the LCEs were taken using a Canon EOS Rebel T3 camera (Canon macro lens EF 100 mm, 1:2.8 USM). The cross-sectional morphology and elemental composition of the LCE film were examined by SEM (Zeiss GeminiSEM 500) equipped with EDS. Before observation, the sample was coated by an 8 nm platinum layer.

X-Ray Scattering: The X-ray scattering measurements were performed at the 9A U-SAXS beamline of the Pohang Accelerator Laboratory (PAL), Korea. 2D scattering patterns were collected using 2D CCD area detector (Rayonix MX170-HS). 1D intensity profiles versus scattering vector $q = (4\pi/\lambda) \sin(\theta/2)$ were obtained from 2D patterns, where θ is the scattering angle and $\lambda = 1.119$ Å ($E = 11.07$ keV) is wavelength of x-ray. The sample-to-detector distances were set as 2.05 and 0.22 m for measurements of small-angle X-ray scattering (SAXS) and WAXS, respectively. The order parameter was calculated using Hermans–Stein orientation distribution function

$$S = \frac{3\langle \cos^2\theta \rangle - 1}{2} \quad (3)$$

$$\langle \cos^2\theta \rangle = \frac{\int_0^{\pi/2} I(\theta) \sin\theta \cos^2\theta d\theta}{\int_0^{\pi/2} I(\theta) \sin\theta d\theta} \quad (4)$$

where θ is the azimuthal angle and $I(\theta)$ is the θ dependent intensity at $q_i = 1.40$ Å.

Gel Fraction: The h-LCE was immersed in chloroform for 48 h to extract the uncrosslinked parts, and then dried in a vacuum oven for 24 h at room temperature to evaporate the remaining solvent. The gel fraction (G) was calculated using the following equation

$$G(\%) = \frac{m_f}{m_i} \times 100\% \quad (5)$$

where m_i is the mass of h-LCE before immersion in chloroform, and m_f is the mass of h-LCE after drying.

Supporting Information

Supporting Information is available from the Wiley Online Library or from the author.

Acknowledgements

K.K., Y.G., and J.B. contributed equally to this work. The authors thank Sunghyun Huh for helpful discussion. This work was supported by the National Research Foundation of Korea (NRF) grant funded by the Korea government, Ministry of Science and ICT (MSIT) (2019R1C1C1006048 and 2019M3D1A2103918). Y.G. and S.C. acknowledge BK FOUR Program for partial financial support.

Conflict of Interest

The authors declare no conflict of interest.

Data Availability Statement

The data that support the findings of this study are available from the corresponding author upon reasonable request.

Keywords

4D printing, actuators, humidity-responsive actuators, hygroscopic actuation, liquid crystal elastomers

Received: March 7, 2021

Revised: March 16, 2021

Published online: May 2, 2021

- [1] C. Dawson, J. F. V. Vincent, A.-M. Rocca, *Nature* **1997**, 390, 668.
- [2] S. Armon, E. Efrati, R. Kupferman, E. Sharon, *Science* **2011**, 333, 1726.
- [3] R. Elbaum, L. Zaltzman, I. Burgert, P. Fratzl, *Science* **2007**, 316, 884.
- [4] D. Evangelista, S. Hotton, J. Dumais, *J. Exp. Biol.* **2011**, 214, 521.
- [5] X. Chen, L. Mahadevan, A. Driks, O. Sahin, *Nat. Nanotechnol.* **2014**, 9, 137.
- [6] a) L. Ionov, *Mater. Today* **2014**, 17, 494; b) J. Shang, X. Le, J. Zhang, T. Chen, P. Theato, *Polym. Chem.* **2019**, 10, 1036; c) M. Jamal, S. S. Kadam, R. Xiao, F. Jivan, T.-M. Onn, R. Fernandes, T. D. Nguyen, D. H. Gracias, *Adv. Healthcare Mater.* **2013**, 2, 1142; d) X. Peng, T. Liu, Q. Zhang, C. Shang, Q.-W. Bai, H. Wang, *Adv. Funct. Mater.* **2017**, 27, 1701962.
- [7] a) B. E. Trembl, R. N. McKenzie, P. Buskohl, D. Wang, M. Kuhn, L.-S. Tan, R. A. Vaia, *Adv. Mater.* **2018**, 30, 1705616; b) H. Arazoe, D. Miyajima, K. Akaike, F. Araoka, E. Sato, T. Hikima, M. Kawamoto, T. Aida, *Nat. Mater.* **2016**, 15, 1084; c) L. Zhang, X. Qiu, Y. Yuan, T. Zhang, *ACS Appl. Mater. Interfaces* **2017**, 9, 41599; d) G. Wang, H. Xia, X.-C. Sun, C. Lv, S.-X. Li, B. Han, Q. Guo, Q. Shi, Y.-S. Wang, H.-B. Sun, *Sens. Actuators, B* **2018**, 255, 1415; e) A. Le Duigou, G. Chabaud, F. Scarpa, M. Castro, *Adv. Funct. Mater.* **2019**, 29, 1903280.
- [8] T. Wu, J. Li, J. Li, S. Ye, J. Wei, J. Guo, *J. Mater. Chem. C* **2016**, 4, 9687.
- [9] a) S. Park, J. An, J. W. Suk, R. S. Ruoff, *Small* **2010**, 6, 210; b) D.-D. Han, Y.-Q. Liu, J.-N. Ma, J.-W. Mao, Z.-D. Chen, Y.-L. Zhang, H.-B. Sun, *Adv. Mater. Technol.* **2018**, 3, 1800258; c) C. Xiang, W. Wang, Q. Zhu, D. Xue, X. Zhao, M. Li, D. Wang, *ACS Appl. Mater. Interfaces* **2020**, 12, 3245; d) G. Xu, M. Zhang, Q. Zhou, H. Chen, T. Gao, C. Li, G. Shi, *Nanoscale* **2017**, 9, 17465; e) W. Wang, C. Xiang, Q. Zhu, W. Zhong, M. Li, K. Yan, D. Wang, *ACS Appl. Mater. Interfaces* **2018**, 10, 27215.
- [10] W. Wang, L. Yao, C.-Y. Cheng, T. Zhang, H. Atsumi, L. Wang, G. Wang, O. Anilonyte, H. Steiner, J. Ou, K. Zhou, C. Wawrousek, K. Petrecca, A. M. Belcher, R. Karnik, X. Zhao, D. I. C. Wang, H. Ishii, *Sci. Adv.* **2017**, 3, e1601984.
- [11] M. Boudot, H. Elettro, D. Grosso, *ACS Nano* **2016**, 10, 10031.
- [12] a) B. Gu, C. Y. Aung, P. H. J. Chong, Y. L. Guan, K. Yong, *IEEE Sens. J.* **2018**, 18, 1081; b) D.-D. Han, Y.-L. Zhang, J.-N. Ma, Y. Liu, J.-W. Mao, C.-H. Han, K. Jiang, H.-R. Zhao, T. Zhang, H.-L. Xu, H.-B. Sun, *Adv. Mater. Technol.* **2017**, 2, 1700045.
- [13] a) S. He, P. Chen, L. Qiu, B. Wang, X. Sun, Y. Xu, H. Peng, *Angew. Chem., Int. Ed.* **2015**, 54, 14880; b) M. Weng, P. Zhou, L. Chen, L. Zhang, W. Zhang, Z. Huang, C. Liu, S. Fan, *Adv. Funct. Mater.* **2016**, 26, 7244.
- [14] A. Holstov, B. Bridgens, G. Farmer, *Constr. Build. Mater.* **2015**, 98, 570.
- [15] a) Y. Zhong, F. Zhang, M. Wang, C. J. Gardner, G. Kim, Y. Liu, J. Leng, S. Jin, R. Chen, *Sci. Rep.* **2017**, 7, 44208; b) T. Jia, Y. Wang, Y. Dou, Y. Li, M. Jung de Andrade, R. Wang, S. Fang, J. Li, Z. Yu, R. Qiao, Z. Liu, Y. Cheng, Y. Su, M. Minary-Jolandan, R. H. Baughman, D. Qian, Z. Liu, *Adv. Funct. Mater.* **2019**, 29, 1808241; c) J. Mu, G. Wang, H. Yan, H. Li, X. Wang, E. Gao, C. Hou, A. T. C. Pham, L. Wu, Q. Zhang, Y. Li, Z. Xu, Y. Guo, E. Reichmanis, H. Wang, M. Zhu, *Nat. Commun.* **2018**, 9, 590.

- [16] a) B. Shin, J. Ha, M. Lee, K. Park, G. H. Park, T. H. Choi, K.-J. Cho, H.-Y. Kim, *Sci. Rob.* **2018**, 3, eaar2629; b) B. Li, T. Du, B. Yu, J. van der Gucht, F. Zhou, *Small* **2015**, 11, 3494; c) S. Taccola, F. Greco, E. Sinibaldi, A. Mondini, B. Mazzolai, V. Mattoli, *Adv. Mater.* **2015**, 27, 1668.
- [17] a) X. Chen, D. Goodnight, Z. Gao, A. H. Cavusoglu, N. Sabharwal, M. DeLay, A. Driks, O. Sahin, *Nat. Commun.* **2015**, 6, 7346; b) Z. Ren, Y. Ding, J. Nie, F. Wang, L. Xu, S. Lin, X. Chen, Z. L. Wang, *ACS Appl. Mater. Interfaces* **2019**, 11, 6143; c) W. Wang, C. Xiang, Q. Liu, M. Li, W. Zhong, K. Yan, D. Wang, *J. Mater. Chem. A* **2018**, 6, 22599.
- [18] a) T. J. White, D. J. Broer, *Nat. Mater.* **2015**, 14, 1087; b) R. S. Kularatne, H. Kim, J. M. Boothby, T. H. Ware, *J. Polym. Sci., Part B: Polym. Phys.* **2017**, 55, 395; c) C. Ohm, M. Brehmer, R. Zentel, *Adv. Mater.* **2010**, 22, 3366.
- [19] a) M. Dai, O. T. Picot, J. M. N. Verjans, L. T. de Haan, A. P. H. J. Schenning, T. Peijs, C. W. M. Bastiaansen, *ACS Appl. Mater. Interfaces* **2013**, 5, 4945; b) L. T. de Haan, J. M. N. Verjans, D. J. Broer, C. W. M. Bastiaansen, A. P. H. J. Schenning, *J. Am. Chem. Soc.* **2014**, 136, 10585; c) A. Ryabchun, F. Lancia, A.-D. Nguindjel, N. Katsonis, *Soft Matter* **2017**, 13, 8070; d) R. C. P. Verpaalen, M. G. Debije, C. W. M. Bastiaansen, H. Halilović, T. A. P. Engels, A. P. H. J. Schenning, *J. Mater. Chem. A* **2018**, 6, 17724; e) R. Lan, J. Sun, C. Shen, R. Huang, L. Zhang, H. Yang, *Adv. Funct. Mater.* **2019**, 29, 1900013; f) J. M. Boothby, T. H. Ware, *Soft Matter* **2017**, 13, 4349; g) K. D. Harris, C. W. M. Bastiaansen, J. Lub, D. J. Broer, *Nano Lett.* **2005**, 5, 1857; h) O. M. Wani, R. Verpaalen, H. Zeng, A. Priimagi, A. P. H. J. Schenning, *Adv. Mater.* **2019**, 31, 1805985.
- [20] K. D. Harris, C. W. M. Bastiaansen, D. J. Broer, *Macromol. Rapid Commun.* **2006**, 27, 1323.
- [21] R. C. P. Verpaalen, A. E. J. Souren, M. G. Debije, T. A. P. Engels, C. W. M. Bastiaansen, A. P. H. J. Schenning, *Soft Matter* **2020**, 16, 2753.
- [22] Y. Liu, B. Xu, S. Sun, J. Wei, L. Wu, Y. Yu, *Adv. Mater.* **2017**, 29, 1604792.
- [23] a) C. Ohm, C. Serra, R. Zentel, *Adv. Mater.* **2009**, 21, 4859; b) C. Ohm, N. Kapernaum, D. Nonnenmacher, F. Giesselmann, C. Serra, R. Zentel, *J. Am. Chem. Soc.* **2011**, 133, 5305.
- [24] a) J. Naciri, A. Srinivasan, H. Jeon, N. Nikolov, P. Keller, B. R. Ratna, *Macromolecules* **2003**, 36, 8499; b) E.-K. Fleischmann, F. R. Forst, R. Zentel, *Macromol. Chem. Phys.* **2014**, 215, 1004; c) S. Nocentini, D. Martella, D. S. Wiersma, C. Parmeggiani, *Soft Matter* **2017**, 13, 8590; d) D. J. Roach, C. Yuan, X. Kuang, V. C.-F. Li, P. Blake, M. L. Romero, I. Hammel, K. Yu, H. J. Qi, *ACS Appl. Mater. Interfaces* **2019**, 11, 19514.
- [25] a) T. H. Ware, M. E. McConney, J. J. Wie, V. P. Tondiglia, T. J. White, *Science* **2015**, 347, 982; b) S.-k. Ahn, T. H. Ware, K. M. Lee, V. P. Tondiglia, T. J. White, *Adv. Funct. Mater.* **2016**, 26, 5819; c) H. Kim, J. M. Boothby, S. Ramachandran, C. D. Lee, T. H. Ware, *Macromolecules* **2017**, 50, 4267; d) H.-H. Yoon, D.-Y. Kim, K.-U. Jeong, S.-K. Ahn, *Macromolecules* **2018**, 51, 1141; e) H. Tian, Z. Wang, Y. Chen, J. Shao, T. Gao, S. Cai, *ACS Appl. Mater. Interfaces* **2018**, 10, 8307; f) T. Guin, M. J. Settle, B. A. Kowalski, A. D. Augustine, R. V. Beblo, G. W. Reich, T. J. White, *Nat. Commun.* **2018**, 9, 2531.
- [26] a) J. Lee, Y. Guo, Y.-J. Choi, S. Jung, D. Seol, S. Choi, J.-H. Kim, Y. Kim, K.-U. Jeong, S.-K. Ahn, *Soft Matter* **2020**, 16, 2695; b) C. P. Ambulo, J. J. Burroughs, J. M. Boothby, H. Kim, M. R. Shankar, T. H. Ware, *ACS Appl. Mater. Interfaces* **2017**, 9, 37332; c) A. Kotikian, R. L. Truby, J. W. Boley, T. J. White, J. A. Lewis, *Adv. Mater.* **2018**, 30, 1706164; d) M. Barnes, S. Sajadi, S. Parekh, M. M. Rahman, P. M. Ajayan, R. Verduzco, *ACS Appl. Mater. Interfaces* **2020**, 12, 28692; e) X. Qian, Q. Chen, Y. Yang, Y. Xu, Z. Li, Z. Wang, Y. Wu, Y. Wei, Y. Ji, *Adv. Mater.* **2018**, 30, 1801103; f) M. Barnes, R. Verduzco, *Soft Matter* **2019**, 15, 870; g) H. Zeng, D. Martella, P. Wasylczyk, G. Cerretti, J.-C. G. Lavocat, C.-H. Ho, C. Parmeggiani, D. S. Wiersma, *Adv. Mater.* **2014**, 26, 2319.
- [27] Y. Guo, J. Lee, J. Son, S.-K. Ahn, J.-M. Y. Carrillo, B. G. Sumpter, *Macromolecules* **2019**, 56, 6878.
- [28] a) T. H. Ware, T. J. White, *Polym. Chem.* **2015**, 6, 4835; b) N. P. Godman, B. A. Kowalski, A. D. Augustine, H. Koerner, T. J. White, *ACS Macro Lett.* **2017**, 6, 1290; c) H.-F. Lu, M. Wang, X.-M. Chen, B.-P. Lin, H. Yang, *J. Am. Chem. Soc.* **2019**, 141, 14364; d) O. Francescangeli, F. Vita, F. Fauth, E. T. Samulski, *Phys. Rev. Lett.* **2011**, 107, 207801.
- [29] a) M. O. Saed, C. P. Ambulo, H. Kim, R. De, V. Raval, K. Searles, D. A. Siddiqui, J. M. O. Cue, M. C. Stefan, M. R. Shankar, T. H. Ware, *Adv. Funct. Mater.* **2019**, 29, 1806412; b) Y. Lee, S. Choi, B. G. Kang, S. K. Ahn, *Materials* **2020**, 13, 3094.
- [30] a) M. A. De Jesús-Téllez, D. M. Sánchez-Cerrillo, P. Quintana-Owen, U. S. Schubert, D. Contreras-López, C. Guerrero-Sánchez, *Macromol. Chem. Phys.* **2020**, 221, 1900543; b) F. A. Plamper, C. V. Synatschke, A. P. Majewski, A. Schmalz, H. Schmalz, A. H. E. Muller, *Polimery-W* **2014**, 59, 66.
- [31] a) V. Chrysostomou, S. Pispas, *J. Polym. Sci., Part A: Polym. Chem.* **2018**, 56, 598; b) N. B. Colthup, *Introduction to Infrared and Raman Spectroscopy*, Academic, San Diego, CA **1975**.
- [32] J. M. Boothby, H. Kim, T. H. Ware, *Sens. Actuators, B* **2017**, 240, 511.
- [33] a) M. López-Valdeolivas, D. Liu, D. J. Broer, C. Sánchez-Somolinos, *Macromol. Rapid Commun.* **2018**, 39, 1700710; b) D. J. Roach, X. Kuang, C. Yuan, K. Chen, H. J. Qi, *Smart Mater. Struct.* **2018**, 27, 125011; c) C. Zhang, X. Lu, G. Fei, Z. Wang, H. Xia, Y. Zhao, *ACS Appl. Mater. Interfaces* **2019**, 11, 44774; d) X. Lu, C. P. Ambulo, S. Wang, L. K. Rivera-Tarazona, H. Kim, K. Searles, T. H. Ware, *Angew. Chem., Int. Ed.* **2021**, 60, 5536; e) L. Ren, B. Li, Y. He, Z. Song, X. Zhou, Q. Liu, L. Ren, *ACS Appl. Mater. Interfaces* **2020**, 12, 15562; f) M. del Pozo, L. Liu, M. Pilz da Cunha, D. J. Broer, A. P. H. J. Schenning, *Adv. Funct. Mater.* **2020**, 30, 2005560; g) Z. Wang, Z. Wang, Y. Zheng, Q. He, Y. Wang, S. Cai, *Sci. Adv.* **2020**, 6, eabc0034.
- [34] L. Wu, H. Ma, X. Lu, Y. Wang, Y. Wang, Y. Li, *J. Macromol. Sci., Part A* **2014**, 51, 27.
- [35] Y. Ma, J. Sun, *Chem. Mater.* **2009**, 21, 898.
- [36] a) C. Yao, Z. Liu, C. Yang, W. Wang, X.-J. Ju, R. Xie, L.-Y. Chu, *Adv. Funct. Mater.* **2015**, 25, 2980; b) J. C. Breger, C. Yoon, R. Xiao, H. R. Kwag, M. O. Wang, J. P. Fisher, T. D. Nguyen, D. H. Gracias, *ACS Appl. Mater. Interfaces* **2015**, 7, 3398.